

## Probing Cosmic Plasma with Giant Pulses from the Crab Nebula Pulsar

A. G. Rudnitskii\*, M. V. Popov\*\*, and V. A. Soglasnov\*\*\*

*Astro Space Center, Lebedev Physical Institute, Russian Academy of Sciences,  
Profsoyuznaya ul. 84/32, Moscow, 117997 Russia*

Received July 29, 2016; in final form, September 12, 2016

**Abstract**—A review and comparative analysis of results from studies of the effects of scattering on the interstellar medium using giant pulses of the Crab Nebula pulsar (B0531+21) are presented. This analysis was based on eight epochs of Very Long Baseline Interferometry (VLBI) radio observations carried out as part of the scientific program of the RadioAstron mission during 2011–2015. The scintillation timescale  $t_{\text{scint}}$  and spectral index  $\gamma$  for the power-law energy distribution of the pulses were obtained for each observing epoch. The measured scintillation timescales are  $t_{\text{scint}} = 7.5\text{--}123$  s at 1668 MHz and  $t_{\text{scint}} = 2.9$  s at 327 MHz. The spectral indices are  $-1.6 \dots -2.5$ . The frequency and time characteristics of the scattering were measured using two independent methods: based on the decorrelation bandwidth  $\Delta\nu_d$  and the scattering timescale  $\tau_{\text{SC}}$ . The angular size of the scattering disk  $\theta_{\text{H}}$  of the pulsar was obtained, the phase structure functions constructed, and the distance to the effective scattering screen estimated. The derived diameter of the scattering disk  $\theta_{\text{H}}$  at 1668 MHz ranges from 0.4 to 1.3 mas, while the scattering-disk diameter at 327 MHz is 14.0 mas. The measured distance to the effective scattering screen ranges from 0.7 to 1.9 kpc, and varies from observation to observation in the same way as the scattering timescale and decorrelation bandwidth:  $\tau_{\text{SC}} \approx 0.9\text{--}5.8 \mu\text{s}$  and  $\Delta\nu_d \approx 40.7\text{--}161$  kHz at 1668 MHz. The scattering timescale and decorrelation bandwidth at 327 MHz are 2340  $\mu\text{s}$  and 68 Hz.

**DOI:** 10.1134/S1063772917050043

### 1. INTRODUCTION

The scattering of radio waves from spatially coherent sources, such as pulsars, on inhomogeneities of the interstellar plasma results in effective multi-beam interference, creating diffractive distortions in the spectrum and intensity of the radio emission at the reception point [1, 2]. The distortions in the spectra of pulsars are characterized by the frequency scale  $\Delta\nu_d$  (decorrelation bandwidth). The observed scattering effects also depend on the observing frequency. It was shown for the Crab Nebula pulsar that the time scale  $\tau_{\text{SC}} \propto \nu^{-3.58}$  and the angular size of the scattering disk  $\theta_{\text{H}} \propto \nu^{-1.66}$  [17].

Due to their ultracompact sizes, pulsars afford efficient opportunities for analysis of the properties of ionized plasma in the Galaxy via measurements of scattering effects. It is usual to interpret the basic properties of scattering in a model with homogeneous, isotropic turbulence in the interstellar medium with a Kolmogorov spectrum [3–5]. Studies of the effects of scattering on observations of pulsars have

shown that models with a homogeneous medium are seldom adequate; in most cases, a model with a thin scattering screen is more appropriate [6, 7]. The presence of inhomogeneities in the interstellar plasma is indicated by anomalous scattering phenomena (extreme scattering events, ESEs), which are frequently observed for compact extragalactic sources [8–10]. Evidence for the presence of anisotropy is also provided by VLBI observations [11]; VLBI observations also enable measurement of the angular size of the scattering disk [12].

Special opportunities are afforded by the RadioAstron ground–space interferometer, which provides angular resolutions as high as 1 mas at meter wavelengths (92 cm) and 0.2 mas at decimeter wavelengths (18 cm). This interferometer was used to measure the angular diameters of the scattering disks of the pulsars B0329+54, B1641–45, B1749–28, and B1933+16 and the distances to the effective scattering screens [13, 14]. Layers of scattering plasma near the Sun (10–100 pc) were detected toward the pulsars B0950+08 and B1919+21, which could be responsible for rapid variability in compact extragalactic sources [15, 16].

\*E-mail: [almax1024@gmail.com](mailto:almax1024@gmail.com)

\*\*E-mail: [mwpopov@gmail.com](mailto:mwpopov@gmail.com)

\*\*\*E-mail: [vsoglasn@asc.rssi.ru](mailto:vsoglasn@asc.rssi.ru)

Here, we summarize the results of our analysis of VLBI observations of giant pulses of the Crab Nebula pulsar obtained at 1668 and 327 MHz as part of studies of the effects of scattering in the RadioAstron project. The main parameters (the scattering timescale  $\tau_{\text{SC}}$  and  $\Delta\nu_{\text{d}}$ ) were estimated using two independent methods, enabling us to perform a comparative analysis. We studied the influence of scattering effects on the phase of the visibility function, based on an analysis of phase structure functions. Preliminary results of all these studies were published earlier [17].

## 2. DETERMINATION OF THE MAIN PARAMETERS

The main product of the preliminary processing of VLBI observations (the correlator output) is a set of autocorrelation and cross-correlation spectra (ACs and CCs, respectively), which can be represented in general form as

$$V_{ij}(\nu) = \int_{-\infty}^{+\infty} V_{ij}(\tau) e^{-i\nu\tau} d\tau, \quad (1)$$

where the subscripts  $i$  and  $j$  denote different telescopes (the ACS is obtained when  $i = j$ ), and  $V_{ij}(\tau)$  is the cross-correlation function (CCF), or visibility function:

$$V_{ij}(\tau) = \int_{-T/2}^{T/2} E_i(t) E_j^*(t + \tau) dt. \quad (2)$$

In the case  $i = j$ , the autocorrelation function (ACF) is obtained.

The visibility function is a complex quantity. We analyzed the amplitude  $|V(\tau)|$  and phase  $\varphi(\tau)$  of this complex function, where  $|V(\tau)| = \sqrt{R(\tau)^2 + I(\tau)^2}$  and  $\varphi(\tau) = \arctan \frac{I(\tau)}{R(\tau)}$ , and  $R(\tau)$  and  $I(\tau)$  are the real and imaginary parts of  $V(\tau)$ .

Let us now turn to the observed effects of scattering. We first consider a simple model when scattering takes place during the propagation of coherent radio emission from a pulsar through inhomogeneities of the electron density  $n_e$  with characteristic scale  $a$ , and the spectrum of these inhomogeneities has a Gaussian shape with a maximum at the spatial frequency  $1/a$  [18, 19]. After traversing a distance  $D$  from the pulsar toward the observer the beams encounter a number  $D/a$  such inhomogeneities, resulting in fluctuations of the phase with the root-mean-square (rms) value

$$\Delta\varphi = \frac{2e^2}{m_e c} \frac{\sqrt{aD}}{\nu} \Delta n_e, \quad (3)$$

where  $e$  is the electron charge,  $m_e$  the electron mass,  $c$  the speed of light,  $\nu$  the frequency at which the observations are conducted, and  $\Delta n_e$  the electron-density fluctuations.

The beams are delayed, depending on their refraction angles relative to the directly propagating beams that were not subject to scattering. As a result, instead of a point source, the observer sees a disk of scattered emission with the characteristic angular half-diameter  $\theta_{\text{H}}$ :

$$\theta_{\text{H}} \approx \frac{e^2}{2\pi m_e} \frac{\Delta n_e}{\nu^2} \sqrt{\frac{D}{a}}. \quad (4)$$

The delay time of the beam (the scattering timescale  $\tau_{\text{SC}}$ ) is defined as

$$\tau_{\text{SC}} = \frac{\theta_{\text{H}}^2 D}{c} \approx \frac{1}{ac} \frac{e^4 \Delta n_e^2 D^2}{4\pi^2 m_e^2 \nu^4}. \quad (5)$$

A pulsar pulse recorded by the observer will have an exponential shape with characteristic scale  $\tau_{\text{SC}}$ .

We will also consider the effect of scintillation—a change in the pulsar’s emission intensity that arises during the interference of the direct and scattered beams. Interference of the beams forms a pattern at the plane of the observer consisting of spots with various intensities. This pattern moves in the plane of the observer due to the relative motion of the pulsar, interstellar medium, and observer. As a result, the intensity changes on the timescale  $t_{\text{scint}}$  (the scintillation timescale), and depends on the relative velocity of the motion. The changes in the intensity take place in a restricted frequency band  $\Delta\nu_{\text{d}}$ . This frequency interval (decorrelation bandwidth) is defined as

$$\Delta\nu \approx 8\pi ac \frac{m_e^2}{\Delta n_e^2 e^2} \frac{\nu^4}{D^2}. \quad (6)$$

The signals recorded in a time  $\tau_{\text{SC}}$  have a set of phases  $\Delta\varphi \sim 2\pi\Delta\nu_{\text{d}}\tau_{\text{SC}}$ . Interference of beams is possible when the phases of their waves differ by no more than one radian. Thus, the requirement for interference is  $2\pi\Delta\nu_{\text{d}}\tau_{\text{SC}} = 1$ , relating the decorrelation bandwidth and scattering timescale.

Expressions (4)–(6) show that the scattering timescale  $\tau_{\text{SC}}$ , angular size  $\theta_{\text{H}}$ , and decorrelation bandwidth  $\Delta\nu_{\text{d}}$  have power-law dependences on the observing frequency  $\nu$ . In this simple model, these dependences are:  $\Delta\nu_{\text{d}} \propto \nu^4$  for the decorrelation bandwidth,  $\tau_{\text{SC}} \propto \nu^{-4}$  for the scattering timescale, and  $\theta_{\text{H}} \propto \nu^{-2}$  for the angular size of the scattering disk.

For an arbitrary power-law spectrum for the density inhomogeneities  $P(q) \approx q^{-\beta}$ , defining the index  $\alpha = \beta/(\beta - 2)$ , the frequency dependence of the scattering parameters can be written  $\theta_{\text{H}} \propto \nu^{-\alpha}$ ,  $\tau_{\text{SC}} \propto \nu^{-2\alpha}$ ,  $\Delta\nu_{\text{d}} \propto \nu^{2\alpha}$ .

Now, considering the general case for the distribution of the scattering material along the observer–pulsar line of sight, the following relations are valid for the angular size  $\theta_H$  and scattering timescale  $\tau_{SC}$  [20]

$$\theta_H = \frac{4 \ln 2}{D^2} \int_0^D z^2 \psi(z) dz, \quad (7)$$

$$\tau_{SC} = \frac{1}{2cD} \int_0^D z(D-z) \psi(z) dz, \quad (8)$$

where  $D$  is the distance from the observer to the pulsar,  $z$  the coordinate along the pulsar–observer line of sight, and  $\psi(z)$  the mean scattering angle as a function of  $z$ ; in this case,  $\psi(z) \propto \Delta n_e$ .

If we suppose that the scattering material is concentrated in a thin screen at a distance  $d$  from the observer, then  $\psi(z) \propto \delta(z - D + d)$ , and we obtain for the angular size of the scattered disk

$$\theta_H = \sqrt{8 \ln 2 c \tau_{SC} \frac{(D-d)}{Dd}}, \quad (9)$$

and for the scattering timescale  $\tau_{SC}$

$$\tau_{SC} = \frac{\theta_H^2}{8c \ln 2} \frac{Dd}{(D-d)}. \quad (10)$$

Adopting the parameter  $\alpha_s = d/D$  and knowing the scattering timescale and angular size of the scattered disk, we can find the distance to the scattering screen:

$$\alpha_s = \frac{8c\tau_{SC} \ln 2}{\theta_H^2 D + 8c\tau_{SC} \ln 2}. \quad (11)$$

Finally, the observed size of the diffraction pattern of inhomogeneities of the interstellar medium  $r_{diff}$  can be expressed in this case by the relationship

$$r_{diff} = \sqrt{2 \ln 2} \frac{\lambda}{\pi \theta_H}, \quad (12)$$

where  $\lambda$  is the observing wavelength.

Knowing  $r_{diff}$  and the velocity of the diffraction pattern  $v$ , we can estimate the scintillation timescale of a pulsar:

$$t_{scint} \approx \frac{r_{diff}}{v}. \quad (13)$$

The distance from the observer to the pulsar B0531+21 is well known,  $D = 2$  kpc, and the distance from the observer to the scattering screen can be expressed in terms of the measured parameter  $\alpha_s$

as  $d = \alpha_s D$ . Thus, we can calculate the velocity of the diffraction pattern in the plane of the observer:

$$v = v_p \frac{d}{D-d}, \quad (14)$$

where  $v_p$  is the tangential velocity of the pulsar, which is approximately 150 km/s for the Crab Nebula pulsar.

The angular size of the scattered disk can be measured by analyzing the dependence of the visibility-function amplitude on the projected baseline in VLBI observations [12]:

$$|V_{ij}(B)| = |V(0)| \times \exp \left[ -\frac{1}{2} \left( \frac{\pi}{\sqrt{2 \ln 2}} \frac{\theta_H B}{\lambda} \right)^{\alpha-2} \right], \quad (15)$$

where  $B$  is the projected baseline in wavelengths,  $\alpha$  the index of the inhomogeneity spectrum, and  $\lambda$  the observing wavelength.

All estimates and results presented here were obtained by assuming the presence of a single thin scattering screen. When estimating the angular size of the scattering disk, it was assumed that the inhomogeneity spectrum was Gaussian, i.e.,  $\alpha = 4$ .

### 3. OBSERVATIONS AND DATA PROCESSING

Nine observations of the pulsar B0531+21 were conducted in 2011–2015, of which eight sessions were successful. The list of observations of the Crab pulsar is given in Table 1, which lists the experiment code, date and time of the observations, maximum projected baseline with the space radio telescope (SRT)  $B$  in kilometers, observing wavelength  $\lambda$ , duration of the observations  $T$  in hours, and the number of participating ground-based telescopes (GRTs)  $N_{GRT}$ . Of the eight successful sessions, seven were carried out at 1668 MHz and one at 327 MHz, with a total of 26 hours of observations at 1668 MHz and 12 hours at 327 MHz. A significant interference response with the SRT was detected for the strongest pulses in six sessions, and only for the observations at 1668 MHz. The strongest pulses were recorded in the sessions during 2015 (experiment codes RAGS10A and RAGS10B), with the peak flux density reaching  $10^5$  Jy in some cases.

The data from the telescopes were recorded on data disks in Mark4A/Mark5B/RDR formats. The signals were recorded in two 16-MHz subbands, in left-hand and right-hand circular polarizations (LCP and RCP).

The correlation and preliminary processing of the data were carried out at the Astro Space Center (Lebedev Physical Institute, Russian Academy of

**Table 1.** RadioAstron observations of the pulsar B0531+21 in 2011–2015

Session code	Date	Time	$T$ , h	$B$ , km	$\lambda$ , cm	$N_{\text{GRT}}$	Correlation with SRT
RAFS01	14.11.2011	23:00–00:00	1.0	46 000	18	4	Yes
RAES04A	02.03.2012	13:00–17:00	4.0	145 000	18	8	No
RAES04B	06.03.2012	13:30–17:30	4.0	128 000	18	8	Yes
RAES04D	23.10.2012	07:00–09:00	2.0	113 000	18	7	Yes
RAKS02AD	27.10.2013	06:00–09:00	3.0	150 000	18	4	Yes
RAKS02AE	02.11.2013	19:30–08:40	12.0	57 000	92	5	No
RAGS10A	10.01.2015	22:00–04:00	6.0	153 000	18	5	Yes
RAGS10B	28.01.2015	21:00–03:00	6.0	140 000	18/92	10	Yes

Sciences) [21]. The search for and correlation of giant pulses were conducted using the incoherent dedispersion method, with a subsequent selection of events applying the preset criterion for the signal-to-noise (SNR) in the instantaneous CCF  $\text{SNR} = 6\sigma$ . Spectral resolutions of 1024 and 2048 channels were used at 1668 MHz and 327 MHz, respectively. These values correspond to a range of delays in the visibility function  $\pm T/2 \pm 16$  and  $\pm 32 \mu\text{s}$ , respectively. At the correlator output, the CCS and ACS were formed for each pulse, each baseline, the upper and lower sub-bands, LCP and RCP, and the cross-polarizations. Further, we carried out amplitude normalization and post-correlation analysis of the data, and then analyzed the visibility-function amplitudes  $|V(\tau)|$  ( $\tau$  is the delay) and phases  $\varphi(\tau)$ .

For each epoch, we measured the scattering timescale, decorrelation bandwidth, angular size of the scattering disk, radius of the diffraction spot, and distance to the effective scattering screen. About 6000 giant pulses were detected in the 18 cm and about 500 pulses in the 92 cm observations. This extensive database enabled us to analyze not only scattering effects but also some properties of the giant pulses.

#### 4. ENERGY DISTRIBUTION OF THE PULSES

The CCFs (visibility functions) obtained in the preliminary processing contain information about the power of the recorded signal. To extract this information, we took the maximum amplitude of  $|V_{ij}(\tau)|$  for an arbitrary baseline between telescopes  $i$  and  $j$ , which corresponded to a delay  $\tau = 0$  after the correlation; i.e.,  $|V_{ij}(0)|$ .

In the subsequent reduction, a normalization to the maximum amplitude of the visibility function was applied. For an arbitrary baseline between telescopes  $i$  and  $j$ :

$$|V_{ij^*}(0)| = \frac{|V_{ij}(0)|}{\sqrt{(\sigma_{i,\text{tot}}^2 - \sigma_{i,\text{off}}^2)(\sigma_{j,\text{tot}}^2 - \sigma_{j,\text{off}}^2)}}, \quad (16)$$

where the subscript “tot” corresponds to the signal for a recorded giant pulse and “off” corresponds to a signal outside such a pulse. This reduction procedure is described in more detail in [17].

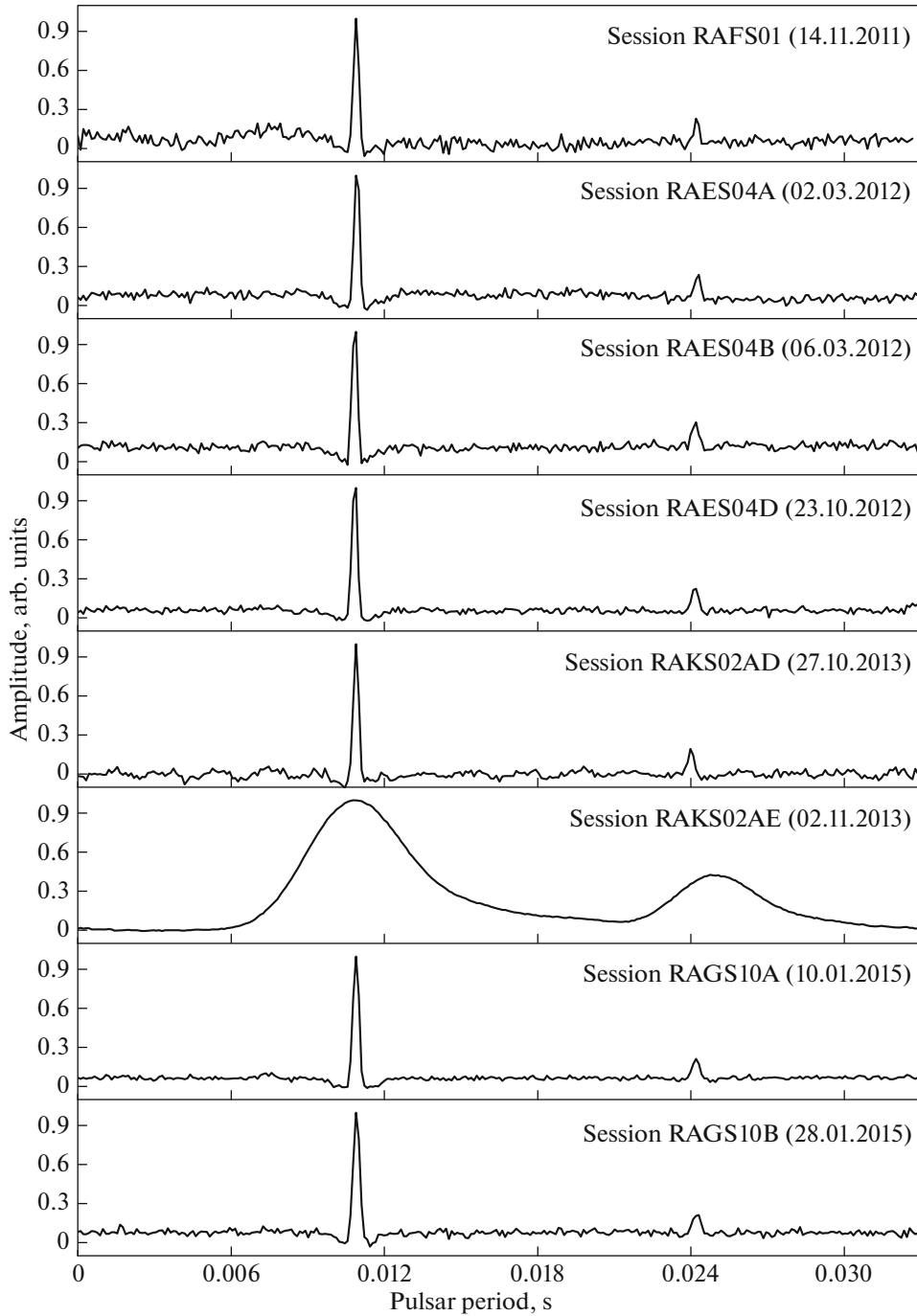
Using the CCFs and the CCSs obtained at the correlator output, we can estimate the energy distribution of the recorded giant pulses. The major advantage of using the CCFs and CCSs is that (1) the noise component in the energy distribution is minimized and (2) the estimate is not tied to the width of the recorded pulse.

Figure 1 shows the mean profiles of the pulsar B0531+21 for each observation obtained on the 70 m telescope in Evpatoria for session RAFS01, on the Westerbork telescope for sessions RAES04A, RAES04B, RAES04D, RAKS02AD, and RAGS10A, on the Effelsberg telescope for session RAGS10B, and on the Arecibo telescope for session RAKS02AE. The effects of scattering are demonstrated more strongly at low frequencies, as can be seen in the mean profile for 327 MHz in Fig. 1.

We realized the translation from the normalized visibility-function amplitude  $|V_{ij^*}(0)|$  to the correlated flux for each baseline using the relationship

$$S_{Jy} = |V_{ij^*}(0)| \sqrt{SEFD_1 SEFD_2}, \quad (17)$$

where  $S_{Jy}$  is the correlated flux in Jansky,  $|V_{ij^*}(0)|$  is the normalized visibility-function amplitude, and



**Fig. 1.** Mean pulse profiles of B0531+21 for eight observations. All sessions were conducted at 18 cm, except for the session RAKS02AE (92 cm). The amplitude of the mean profile is in arbitrary units normalized to the maximum amplitude of the main pulse.

$SEFD_1$  and  $SEFD_2$  are the system equivalent flux densities (SEFDs) for the two telescopes in Janskys, which characterize the sensitivity of the telescopes. The SEFDs for the telescopes also take into account the contribution from the Crab Nebula, which, we estimated to be 165 Jy for the Westerbork telescope, 275 Jy for the Arecibo telescope, and  $\sim 830$  Jy at

1668 MHz and  $\sim 1090$  Jy at 327 MHz for the remaining telescopes.

The energy distribution of the giant pulses has a power-law character,  $N(E) \propto E^\gamma$ :

$$N(E > E_\gamma) = \int_{E_\gamma}^{\infty} n(E) dE \propto E_\gamma^{-\beta+1}, \quad (18)$$

**Table 2.** Measured parameters

Session code	$\tau_{\text{SC}}, \mu\text{s}$	$\theta_{\text{H}}, \text{mas}$	$\Delta\nu_{\text{d}}, \text{kHz}$	$r_{\text{diff}}, \text{km}$	$\alpha_{\text{s}}$	$\gamma$	$t_{\text{scint}}, \text{s}$	Number of GPs
RAFS01	$0.9 \pm 0.1$	$1.3 \pm 0.2$	$116.3 \pm 24.5$	$10\,361 \pm 1700$	$0.36 \pm 0.08$	—	$123.3 \pm 20.2$	98
RAES04A	$5.8 \pm 0.3$	$0.6 \pm 0.1$	$55.2 \pm 5.9$	$21\,817 \pm 2900$	$0.94 \pm 0.02$	$-2.48 \pm 0.01$	$9.3 \pm 1.2$	1202
RAES04B	$5.5 \pm 0.7$	$0.5 \pm 0.1$	$41.2 \pm 7.9$	$26\,949 \pm 7700$	$0.96 \pm 0.03$	$-2.06 \pm 0.01$	$7.5 \pm 2.1$	1034
RAES04D	$5.1 \pm 0.5$	$1.2 \pm 0.1$	$40.7 \pm 4.6$	$11\,413 \pm 900$	$0.79 \pm 0.03$	$-1.64 \pm 0.01$	$20.2 \pm 1.6$	929
RAKS02AD	$2.2 \pm 0.3$	$1.2 \pm 0.1$	$78.1 \pm 7.9$	$12\,113 \pm 1200$	$0.61 \pm 0.06$	$-1.60 \pm 0.01$	$51.5 \pm 5.1$	453
RAKS02AE	$2340 \pm 23$	$14.0 \pm 1.4$	$0.068 \pm 0.002$	$5140 \pm 500$	$0.92 \pm 0.07$	$-1.63 \pm 0.01$	$2.9 \pm 0.3$	579
RAGS10A	$1.4 \pm 0.2$	$0.4 \pm 0.1$	$161.1 \pm 13.4$	$34\,015 \pm 9268$	$0.91 \pm 0.05$	$-1.63 \pm 0.01$	$22.4 \pm 6.1$	1807
RAGS10B	$1.5 \pm 0.1$	$0.5 \pm 0.1$	$70.2 \pm 8.3$	$25\,675 \pm 4485$	$0.85 \pm 0.04$	$-2.51 \pm 0.01$	$30.2 \pm 5.3$	627

where  $n(E)$  is the number of giant pulses with energy  $E$  and  $\gamma = \beta - 1$ . We analyzed the cumulative probability distributions (CPDs) of the giant pulses over the energy for the main pulse (Fig. 2). The data for the interpulse were not analyzed owing to their smaller statistics. The total energy in units of  $\text{Jy} \times \mu\text{s}$  was calculated as  $S_{Jy} \times \delta t$ , where  $\delta t_{18\text{cm}} = 32 \mu\text{s}$  and  $\delta t_{92\text{cm}} = 64 \mu\text{s}$  are the widths of the correlation windows in microseconds, which were chosen in the correlation processing for 18 cm and 92 cm, and  $S_{Jy}$  is the correlated flux in Jansky.

The index  $\gamma$  was estimated from a power-law fit to the obtained CPD. Table 2 lists the spectral indices for each session. The spectral index was not estimated for session RAFS01 due to the small duration of the session (1 hour), leading to small statistics for the recorded pulses. Estimates of  $\gamma$  in other studies yielded values between  $-1.5$  and  $-3.5$  for various frequency ranges [23, 24]. The results of our estimates are quite consistent with these earlier measurements. The break at low energies was not detected due to the limited sensitivity of the interferometric response. Similar values of the energy distribution index of the pulses were obtained for the millisecond pulsar B1937+21 ( $\gamma \approx -1.4$ , pulse duration  $\approx 1-2 \mu\text{s}$ ) [22].

## 5. SCATTERING TIMESCALE

One of the main parameters describing scattering is the scattering timescale  $\tau_{\text{SC}}$ , brought about by the delays of the scattered beams. The scattering timescale was calculated based on an analysis of the average visibility functions  $\langle |V(\tau)| \rangle$  obtained on the ground-space baselines. In this case, there is no central, compact feature in the temporal structure of the visibility function, only an extended part corresponding to scattering. Thus, the ground-space

observations involving the RadioAstron antenna enabled us to directly measure the scattering timescale via an exponential fit to the visibility function  $\langle |V(\tau)| \rangle$ .

Another method for measuring the scattering timescale was used to check the results obtained using the ground-space baselines, namely, analyzing the average visibility function  $\langle |V(\tau)| \rangle$  for the ground baselines. In this case, the visibility function has at least two features: a narrow, central part corresponding to unresolved structure and a broad portion corresponding to scattering.

Figure 3 shows the average visibility functions for the most sensitive baseline in each session on a semi-log scale. To calculate the scattering timescale, we fitted the sum of an exponential function (extended feature) and a Gaussian (narrow feature) to the visibility functions:

$$|V(\tau)| = V_1 e^{-\frac{|\tau|}{\tau_1}} + V_2 e^{-\frac{\tau^2}{\tau_2}} + V_0. \quad (19)$$

In addition, in all sessions except for RAFS01 (November 14, 2011) and RAGS10B (January 28, 2015), one more exponential scale with the characteristic value  $\tau \sim 100 \text{ ns}$  was detected. In this case, the fitted function became

$$|V(\tau)| = V_1 e^{-\frac{|\tau|}{\tau_1}} + V_2 e^{-\frac{|\tau|}{\tau_2}} + V_3 e^{-\frac{\tau^2}{\tau_3}} + V_0. \quad (20)$$

For the 92 cm session (RAKS02AE), we were able to measure the scattering timescale only from the mean pulse profile (see Fig. 1), via an exponential fit to the extended part of the main pulse or interpulse; this yielded the scattering timescale  $\tau_{\text{SC}} = 2340 \pm 23 \mu\text{s}$ . Assuming that  $2\pi\Delta\nu_{\text{d}}\tau_{\text{SC}} = 1$ , the estimated decorrelation bandwidth is  $\Delta\nu_{\text{d}} = 68 \pm 2 \text{ Hz}$ .

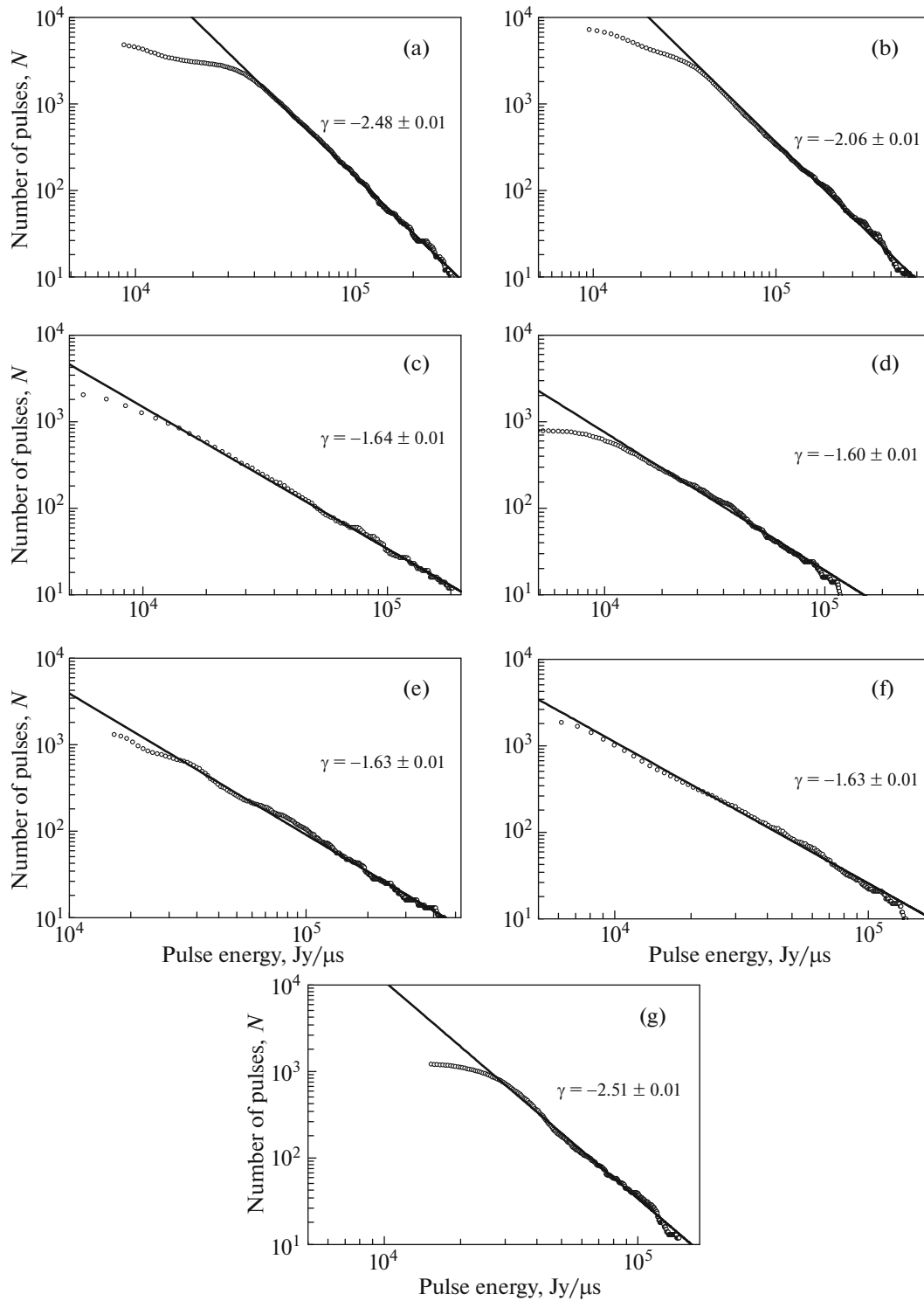


**Fig. 2.** Energy distribution of the giant pulses on a logarithmic scale for session (a) RAES04A (March 2, 2012), (b) RAES04B (March 6, 2012), (c) RAES04D (October 23, 2012), (d) RAKS02AD (October 27, 2013), (e) RAKS02AE (November 2, 2013), (f) RAGS10A (January 10, 2015), and (g) RAGS10B (January 28, 2015). The straight lines show the slopes of the distributions.

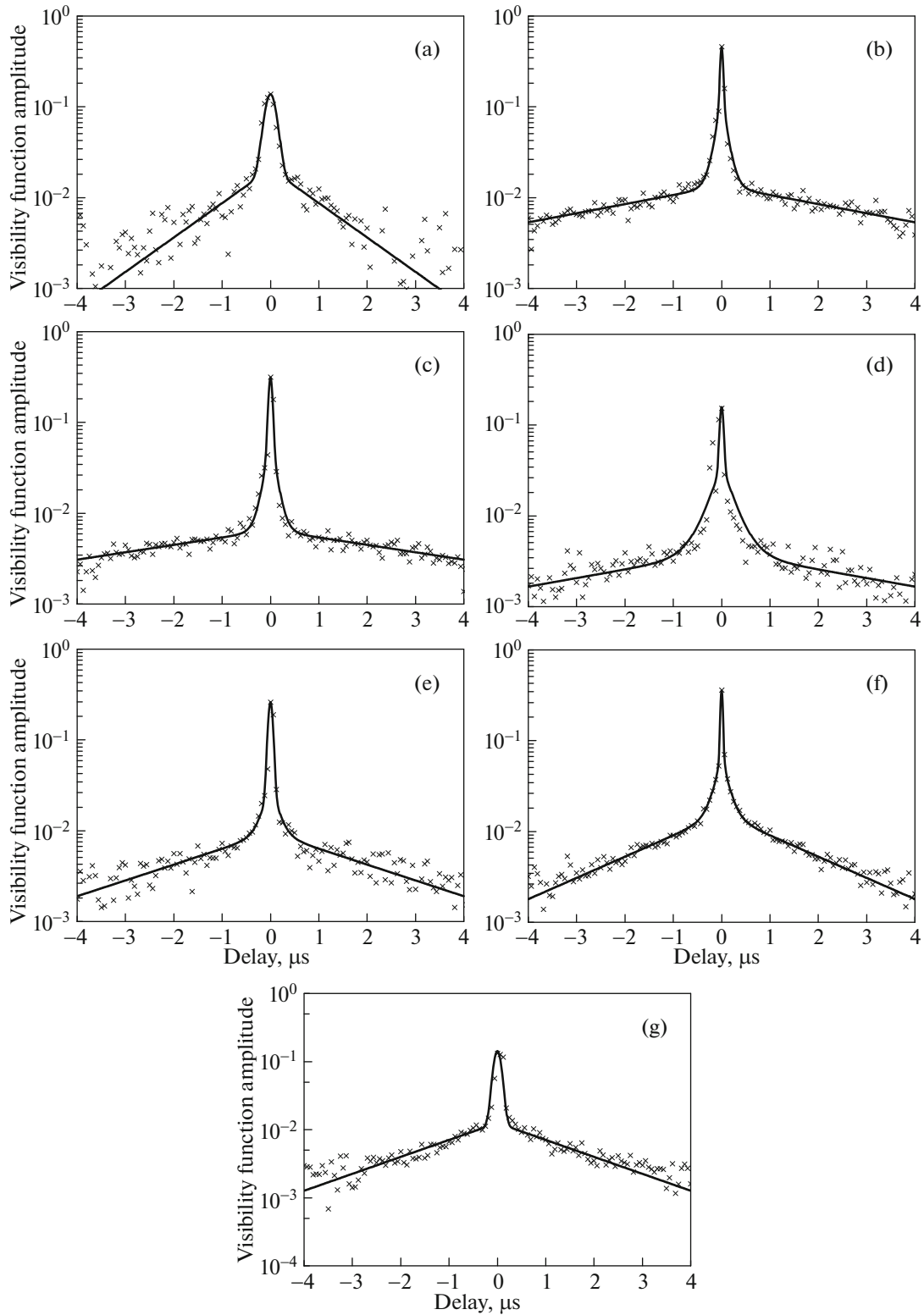


**Fig. 3.** Average visibility functions for the ground baselines for session (a) RAFS01 (November 14, 2011, Svetloe–Evpatoria), (b) RAES04A (March 2, 2012, Effelsberg–Westerbork), (c) RAES04B (March 6, 2012, Effelsberg–Westerbork), (d) RAES04D (October 23, 2012, Effelsberg–Westerbork), (e) RAKS02AD (October 27, 2013, Effelsberg–Westerbork), (f) RAGS10A (January 10, 2015, Westerbork–Arecibo), and (g) RAGS10B (January 28, 2015, Effelsberg–Medicina). The curves show the fits to the average visibility functions.

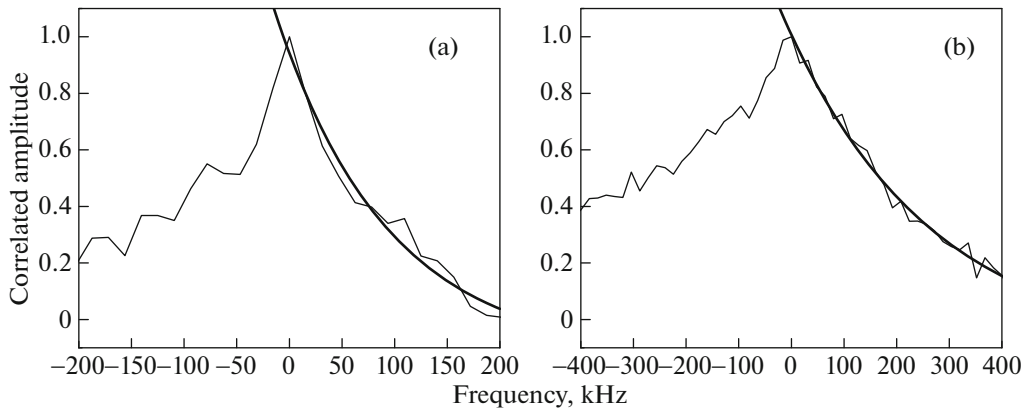


**Fig. 4.** Examples of CCFs for the session RAGS10A (January 10, 2015), obtained by correlating (a) the ACSs of two different telescopes, but in one polarization channel and (b) the ACSs of one telescope, but in the two polarization channels. The curves show the fitted exponential function.

## 6. FREQUENCY SCALE OF THE SCATTERING

Another important parameter of the scattering is the decorrelation bandwidth. This parameter corresponds to the characteristic frequency scale of the distortions in the spectrum produced by scattering. The parameters  $\tau_{SC}$  and  $\Delta\nu$  are related by the expression  $2\pi\Delta\nu_d\tau_{SC} = 1$ .

Figure 4 shows examples of the cross-correlation functions  $CCF(\nu)$  for session RAGS10A, where the CCF was obtained by correlating (a) the ACSs of two different telescopes, but in one polarization channel, and (b) the ACSs of one telescope, but in the two polarization channels. We used these CCFs instead of the ACFs to eliminate the noise peak at zero shift.

The decorrelation bandwidth  $\Delta\nu_d$  was determined from an exponential fit,  $CCF(\nu) = A_0 \exp(-\nu/\Delta\nu_d)$ , obtained by correlating the ACSs from two different radio telescopes in one polarization channel, or the CCFs obtained by correlating two ACSs from one radio telescope, but in the two polarization channels.

## 7. PHASE STRUCTURE FUNCTION

Analysis of the time behaviour of the phase using structure functions is also of interest, and enables additional estimation of the angular size of the scattering disk. We analyzed the phase structure functions of the visibility function during individual giant pulses for the ground baselines.

The value of the visibility function phase  $\varphi(\tau)$  was chosen for the delay with the maximum amplitude  $|V(\tau)|$ ; an additional check was conducted for events (pulses) with poor signal-to-noise levels and events (pulses) that did not yield significant correlations on a particular selected baseline. Such events were

eliminated from consideration. The ground-space baselines were not used in this analysis, since the observed changes in the shape of the visibility function for projected baselines longer than the size of the diffraction spot and the poor signal-to-noise on these baselines hindered unambiguous determination of the channel from the delay in the visibility function for which the phase was to be chosen. In its general form, the phase structure function is defined as

$$D_\varphi(\Delta t) = \langle [\varphi(t) - \varphi(t + \Delta t)]^2 \rangle_{\Delta t}. \quad (21)$$

Further, the phase fluctuations  $\Delta\varphi$  can be obtained from the time dependence of the phase structure function, which corresponds to the square root of the phase structure function at the point with the minimum time.

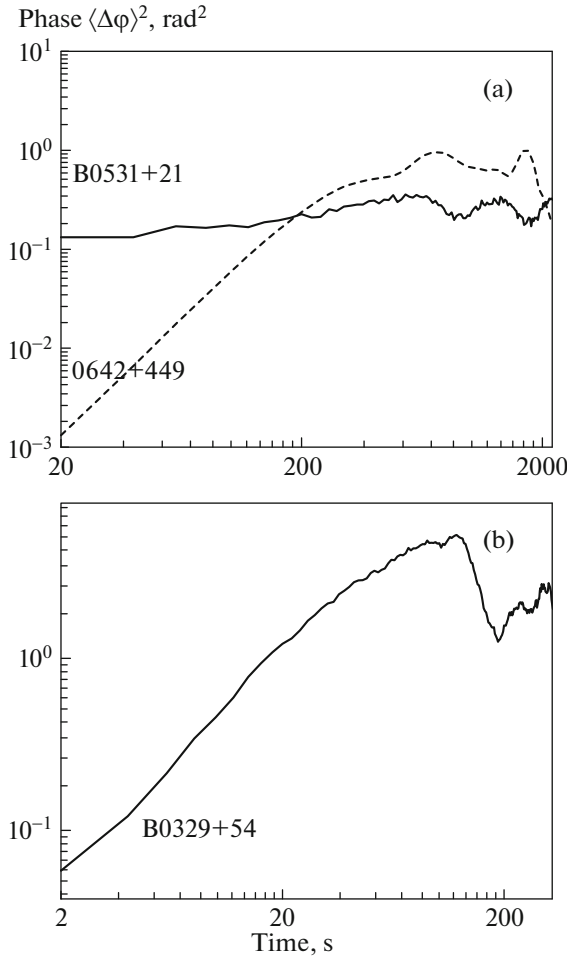
Figure 5a presents the phase structure functions for the pulsar B0531+21 (session RAGS10A) and, for comparison, for the quasar 0642+449 at 18 cm. When calculating the structure functions, we chose the time step  $\Delta t = 20$  s. The root-mean-square phase fluctuations for the pulsar for the minimum shift  $\Delta t$  was  $\langle \Delta\varphi \rangle = 0.42$  rad, and the associated standard deviation  $\sigma_{\Delta\varphi} = 0.12$  rad. The magnitude of the phase fluctuations is considerably smaller for the quasar (Fig. 5a),  $\Delta\varphi = 0.036$  rad. This suggests that the difference in  $\Delta\varphi$  for the quasar and the giant pulses is due to scattering of the pulsar radio emission in the interstellar medium. For large times  $t > 100$  s ( $5\Delta t$ ), similar quasi-periodic large-scale fluctuations of the phase are observed, which are associated with atmospheric and ionospheric perturbations and have characteristic timescales  $t \approx 1000$ – $1200$  s.

Figure 6a shows that  $\Delta\varphi$  does not depend on the projected baseline, making it impossible to estimate the angular size of the scattering disk using the above

**Table 3.** Comparison of the scattering timescale and decorrelation bandwidth for B0531+21 measured using two independent methods

Session code	$\tau_{\text{SC1}}, \mu\text{s}$	$\tau_{\text{SC2}}, \mu\text{s}$	$\Delta\nu_{\text{d1}}, \text{kHz}$	$\Delta\nu_{\text{d2}}, \text{kHz}$
RAFS01	$0.9 \pm 0.1$	$1.1 \pm 0.3$	$116.3 \pm 24.5$	$149.3 \pm 47.6$
RAES04A	$5.8 \pm 0.3$	$4.3 \pm 0.4$	$55.2 \pm 5.9$	$43.5 \pm 5.6$
RAES04B	$5.5 \pm 0.7$	$5.3 \pm 0.6$	$41.2 \pm 7.9$	$57.3 \pm 9.9$
RAES04D	$5.1 \pm 0.5$	$4.6 \pm 0.7$	$40.7 \pm 4.6$	$44.3 \pm 3.8$
RAKS02AD	$2.2 \pm 0.3$	$2.5 \pm 0.2$	$78.1 \pm 7.9$	$140.8 \pm 20.3$
RAGS10A	$1.4 \pm 0.2$	$1.9 \pm 0.2$	$161.1 \pm 13.4$	$279.2 \pm 34.4$
RAGS10B	$1.5 \pm 0.1$	$1.7 \pm 0.6$	$70.2 \pm 8.3$	$192.6 \pm 26.1$

method. This is valid when the baseline projection is less than the diffraction-spot radius,  $r_{\text{diff}} =$



**Fig. 5.** (a) Phase structure function for B0531+21 (session RAGS10A, solid curve) and, for comparison, for the quasar 0642+449 (dashed curve), with a time step  $\Delta t = 20$  s. (b) Phase structure function for the pulsar B0329+54, with a time step  $\Delta t = 2$  s.

$\sqrt{2 \ln 2} \frac{\lambda}{\pi \theta_{\text{H}}}$ . For comparison, a similar analysis of the phase structure functions for the pulsar B0329+54, which also was observed with RadioAstron, was carried out. The diffraction-spot radius for this pulsar at 92 cm was 17 000 km. The average value of the phase fluctuations for projected baselines of 2000 km was  $\Delta\varphi \approx 0.16$ –0.19; for projected baselines more than 15 000–17 000 km, the value of  $\Delta\varphi$  changed with the projected baseline, increasing from 0.25 to 0.33 and then becoming approximately constant for projected baselines great than 18 000 km,  $\Delta\varphi \approx 0.33$  (Fig. 6c).

The magnitude of the phase fluctuation for B0531+21 remains approximately constant with increasing projected baseline, since the diffraction-spot radius varies from 10 000 to 34 000 km at 18 cm, whereas the maximum ground projected baselines did not exceed 9000 km. A change in the phase fluctuations is expected when the projected baseline is close to or larger than the diffraction-spot radius  $r_{\text{diff}}$ . Only then is it possible to estimate the angular size of the scattering disk  $\theta_{\text{H}}$  using relationship (15).

In addition, we used (13) to calculate the scintillation timescale  $t_{\text{scint}}$  for each session (see Table 2). The obtained values are less than or comparable to the time step chosen when constructing the structure function,  $\Delta t = 20$  s. Thus, in the case of B0531+21, the growth segment of the phase structure function is outside  $t_{\text{scint}} < \Delta t$ , the minimum analyzed time interval. The choice of a shorter time step  $\Delta t$  is not possible for this pulsar, first and foremost due to the difficulties in processing data for giant pulses, whose detection rate in the observing sessions was about two to five giant pulses per minute. In contrast, for the pulsar B0329+54, with a scintillation timescale of about  $\approx 100$  s, the phase structure function displays a smooth growth after  $\Delta t = 2$  s, and saturation by a timescale of  $\approx 100$  s (Fig. 5b).

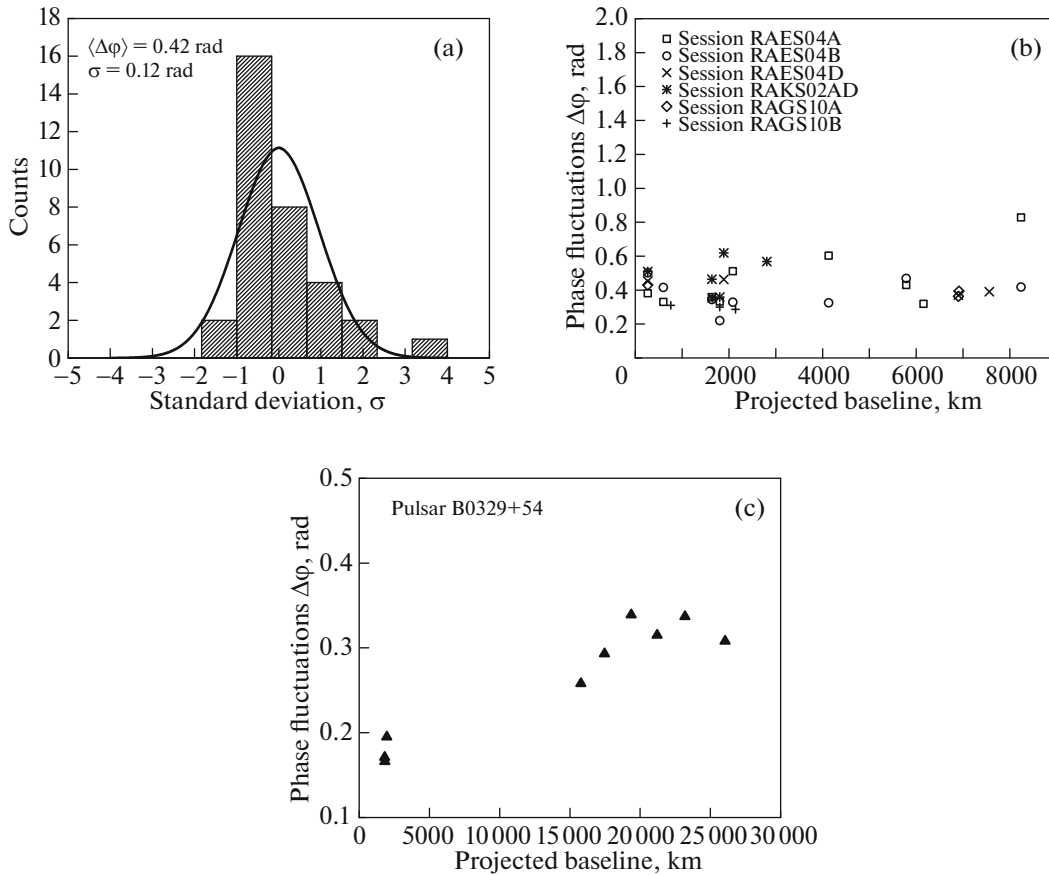


**Fig. 6.** (a) Statistical distribution of the phase fluctuations  $\Delta\varphi$  and (b) dependence of the phase fluctuations  $\Delta\varphi$  on the projected baseline for the Crab pulsar. (c) For comparison, the dependence of the phase fluctuations  $\Delta\varphi$  on the projected baseline for the pulsar B0329+54. The projected baselines are in kilometers.

### 8. CONCLUSION

The computed indices of the pulse energy distribution are  $-1.6 \dots -2.5$ , consistent with values obtained earlier. However, changes in this index from epoch to epoch can be noted.

Table 2 presents a complete list of the derived scattering parameters for all the observing sessions for the pulsar B0531+21 conducted with RadioAstron. The measured scintillation timescales  $t_{\text{scint}}$  are 7.5–120 s for 1668 MHz, and  $2.9 \pm 0.3$  s in the session RAKS02AE at 327 MHz. The decorrelation bandwidth  $\Delta\nu_d$  and scattering timescale  $\tau_{\text{SC}}$  were also measured using two independent methods (see Table 3). The results of these measurements are quite consistent, and the use of two independent methods provided an additional check of the results obtained, giving us confidence in their correctness. At the same time, the calculation of the decorrelation bandwidth using the first method, based on the ACSs from two different telescopes, is preferred, and yields more reliable results [30]. Three timescales were observed when analyzing the visibility functions for the ground

baselines for nearly all sessions at 18 cm: a narrow scale corresponding to a central unresolved component, an extended scale corresponding to scattering, and an intermediate scale with a characteristic time of 90–100 ns.

The scattering timescale for the 92-cm observations could be estimated from the broadening of the mean profile of the pulsar, which yielded  $\tau_{\text{SC}} = 2340 \pm 23 \mu\text{s}$ ; this results in a decorrelation bandwidth  $\Delta\nu_d = 68 \pm 2$  Hz.

Changes in the scattering parameters from epoch to epoch are observed. In particular, as is visible from Table 2, the derived distance to the scattering screen is different for different observing epochs. Our calculations were carried out using a model with a single thin scattering screen, where the position of the screen corresponds to the dominant region of scattering. For instance, in the session of November 14, 2011 (RAFS01), the position of the screen corresponded to a virtually uniform distribution of the scattering material along the line of sight (the case when the distance to the screen is  $d = D/3$ , where  $D$

is the distance to the pulsar [26]). At the same time, in many other sessions, the screen position was in the vicinity of the Crab Nebula. We conclude that a model with a single thin screen is too simple to adequately describe the distribution of the scattering material along the line of sight toward the Crab pulsar, making it necessary to use a model with several scattering screens or a superposition of a single screen and material distributed uniformly along the line of sight. Nevertheless, the observed epoch-to-epoch variation in the screen position testifies to the dominant influence of the Crab Nebula on the scattering of the radio emission from B0531+21. The position of the effective scattering screen was close to the nebula in a period of “strong” scattering (see [17, 27]). Crossley et al. [28] and Kuzmin et al. [29] also concluded that the Crab Nebula dominated the observed scattering of the pulsar radio emission.

Our analysis of the phase fluctuations based on the phase structure functions for ground baselines for the 18-cm sessions showed that these phase fluctuations are virtually constant with increasing projected baseline when the projected baselines are less than the radius of the diffraction spot. At the same time, a similar analysis for another pulsar, B0329+54, showed a change in the phase fluctuations for projected baselines exceeding the radius of the diffraction spot. The presence of quasi-regular phase fluctuations in the structure function with a characteristic timescale of about 1000–1200 s was also noted, which could be due to atmospheric and ionospheric perturbations.

The measured appreciable fluctuations of the visibility function phase  $\varphi(\tau)$ , compared to the continuum source 0642+449, can be explained by the influence of diffraction distortions of the radio spectra of individual pulses due to scintillations, as well as fine structure in the giant pulses, as has been shown in [30].

#### ACKNOWLEDGMENTS

The authors are grateful to T.V. Smirnova, V.I. Shishov, A. Andrianov, C. Gwinn, and E. Fadeev for useful comments and suggestions during the preparation of the article. This work was supported by Program P7 of the Presidium of the Russian Academy of Sciences.

The RadioAstron project is realized by the Astro Space Center, Lebedev Physical Institute, Russian Academy of Sciences and the S.A. Lavochkin Science and Production Association, under contract with the Russian Space Agency, together with many scientific and technological organizations in Russia and other countries. The results presented here are based partially on observations carried out at radio telescopes of the Institute of Applied Astronomy of the Russian Academy of Sciences.

#### REFERENCES

1. P. A. G. Scheuer, *Nature* **218**, 920 (1968).
2. B. J. Rickett, *Ann. Rev. Astron. Astrophys.* **15**, 479 (1977).
3. J. W. Armstrong, B. J. Rickett, and S. R. Spangler, *Astrophys. J.* **443**, 209 (1995).
4. B. J. Rickett, *Ann. Rev. Astron. Astrophys.* **28**, 561 (1990).
5. R. Narayan, *Philos. Trans.: Math., Phys. Eng. Sci.* **341**, 151 (1992).
6. M. L. Putney and D. L. Stinebring, *Chin. J. Astron. Astrophys. Suppl.* **6**, 233 (2005).
7. B. Rickett, S. Johnston, T. Tomlinson, and J. Reynolds, *Mon. Not. R. Astron. Soc.* **395**, 1391 (2009).
8. R. L. Fiedler, B. Dennison, K. J. Johnston, and A. Hewish, *Nature* **326**, 675 (1987).
9. T. J. W. Lazio, E. B. Waltman, F. D. Ghigo, R. L. Fiedler, R. S. Foster, and K. J. Johnston, *Astrophys. J. Suppl. Ser.* **136**, 265 (2001).
10. C. E. Senkbeil, S. P. Ellingsen, J. E. J. Lovell, J. P. Macquart, G. Cimo, and D. L. Jauncey, *Astrophys. J. Lett.* **672**, L95 (2008).
11. K. M. Desai and A. L. Fey, *Astrophys. J. Suppl. Ser.* **133**, 395 (2001).
12. C. R. Gwinn, N. Bartel, and J. M. Cordes, *Astrophys. J.* **410**, 673 (1993).
13. M. V. Popov, A. S. Andrianov, N. Bartel, C. R. Gwinn, et al., *Astrophys. J.* **822**, 96 (2016).
14. M. V. Popov, A. S. Andrianov, N. Bartel, C. Gwinn, B. C. Joshi, D. Jauncey, N. S. Kardashev, A. G. Rudnitskii, T. V. Smirnova, V. A. Soglasnov, E. N. Fadeev, and V. I. Shishov, *Astron. Rep.* **60**, 792 (2016).
15. T. V. Smirnova, V. I. Shishov, M. V. Popov, C. R. Gwinn, et al., *Astrophys. J.* **786**, 115 (2014).
16. V. I. Shishov, T. V. Smirnova, C. R. Gwinn, A. S. Andrianov, M. V. Popov, A. G. Rudnitskiy, and V. A. Soglasnov, *Mon. Not. R. Astron. Soc.* (in press).
17. A. G. Rudnitskii, R. Karuppusamy, M. V. Popov, and V. A. Soglasnov, *Astron. Rep.* **60**, 211 (2016).
18. D. R. Lorimer and M. Kramer *Handbook of Pulsar Astronomy* (Cambridge Univ. Press, Cambridge, 2005).
19. R. Manchester and J. Taylor, *Pulsars* (Freeman, San Francisco, 1977; Mir, Moscow, 1980).
20. M. C. Britton, C. R. Gwinn, and M. J. Ojeda, *Astrophys. J.* **501**, L101 (1998).
21. A. S. Andrianov, I. A. Girin, V. E. Zharov, V. I. Kostenko, S. F. Likhachev, and M. V. Shatskaya, *Vestn. NPO im. S.A. Lavochkina* **3**, 55 (2014).

22. V. A. Soglasnov, M. V. Popov, N. Bartel, W. Cannon, A. Yu. Novikov, V. I. Kondratiev, and V. I. Altunin, *Astrophys. J.* **616**, 439 (2004).
23. M. V. Popov and B. Stappers, *Astron. Astrophys.* **470**, 1003 (2007).
24. T. H. Hankins, G. Jones, and J. A. Eilek, *Astrophys. J.* **802**, 130 (2015).
25. V. I. Kondratiev, M. V. Popov, V. A. Soglasnov, Y. Y. Kovalev, N. Bartel, W. Cannon, and A. Y. Novikov, *Astron. Astrophys. Trans.* **26**, 585 (2007).
26. K. M. Desai, C. R. Gwinn, J. Reynolds, E. A. King, et al., *Astrophys. J.* **393**, L75 (1992).
27. R. Karuppusamy, B. W. Stappers, and W. van Straten, *Astron. Astrophys.* **515**, A36 (2010).
28. J. H. Crossley, J. A. Eilek, and T. H. Hankins, *ASP Conf. Ser.* **365**, 271 (2007).
29. A. Kuzmin, B. Ya. Losovsky, C. A. Jordan, and F. G. Smith, *Astron. Astrophys.* **483**, 13 (2008).
30. M. V. Popov, A. G. Rudnitskii, and V. A. Soglasnov, *Astron. Rep.* (in press).

*Translated by G. Rudnitskii*